CONDENSED MATTER PHYSICS

Cooperative and selective redox doping switches single-molecule magnetism

Fabian Paschke[1]*†, Matteo Briganti[2]*†, Vivien Enenkel[1], Tobias Birk[1], Jan Dreiser[3], Peter Schmitt[4], Rainer F. Winter[4], Federico Totti[3]*, Mikhail Fonin[1]*

The controlled manipulation of electronic and magnetic states in single-molecule magnets (SMMs) is crucial for their implementation in molecular electronics, spintronics, and quantum computation. In typical SMMs, key properties like magnetic anisotropy and slow magnetic relaxation are imposed by complex ligand shells, whose bulky and three-dimensional structures hamper efficient manipulation of the molecular magnetism by chemical methods. This work demonstrates highly selective redox doping of an Fe_4 nanomagnet on a Pb(111) surface using lithium atoms. Scanning tunneling microscopy, x-ray absorption spectroscopy, and ab initio calculations reveal the cooperative incorporation of three Li atoms per Fe_4 molecule, resulting in a selective, threefold reduction of its iron-based magnetic core. The doping modifies the intramolecular exchange interaction, turning from antiferromagnetic to ferromagnetic, and changes the molecular magnetic anisotropy from easy-axis to easy-plane. This study demonstrates successful chemical redox doping of individual polynuclear molecular magnets, exploits a rare showcase of cooperative binding, and highlights a route for tuning magnetic properties of complex SMMs.

INTRODUCTION

Finding molecular systems that use functionalities like a switching capability is crucial for developing advanced materials and technologies at the nanometer scale (*1*–*6*). Responsive and adaptive devices such as sensors, data storage units, and neuromorphic or energy-efficient switches need to allow precise control over molecular degrees of freedom (*7*–*9*), i.e., by converting external stimuli into predictable readout states at the single-molecule scale. Atomic doping of an individual molecule can be considered as a cutting-edge alternative "stimulus" to the commonly used external mechanical, electric, magnetic, or photonic triggers (*3*–*5*, *10*–*17*). In such a framework, single-molecule magnets (SMMs) are key candidates to act as functional units (*18*–*23*), in which triggers can be transduced into magnetic output. Despite their functionality, crucial challenges in the view of future applications remain to contact, manipulate, and read out the electronic and magnetic states of SMMs on a local scale.

While successful attempts to contact individual SMMs in scanning probe and break-junction geometries have been reported (*14*, *24*–*27*), the controlled manipulation of their electronic and magnetic properties remains challenging. Recent efforts mainly focused on single-ion, paramagnetic compounds of flat geometry (*28*–*34*), for which electronic doping using alkali metal atoms crystallized as a controllable local manipulation technique (*28*, *30*, *32*). In these doping experiments, changes of the crystal field and spin states upon alkali metal doping were observed for metal phthalocyanines (MPcs) on a Ag(111) surface (*30*, *32*), and quenching of the molecular spin after cesium doping was demonstrated in YPc_2 (*28*). Yet, the desired properties of SMMs, like inherent magnetic anisotropy and slow magnetic relaxation, often rely on a complex three-dimensional ligand shell, which complicates investigation on a single-molecule scale for several reasons. First, their intricate electronic structure hampers the understanding of doping effects; second, these naturally bulky compounds lack defined adsorption configurations for the alkali atoms; and third, the large ligands shield the spin-carrying centers from the dopants. To the best of our knowledge, no attempt has yet been reported to implement alkali metal doping for the manipulation of charge or spin states of large, polynuclear SMMs. Few experiments exist that explore alkali metal doping of nonplanar compounds, particularly attachment of K and Cs atoms to bulky, albeit nonmagnetic C_{60} cages (*35*–*37*). In these experiments, doping resulted in sample inhomogeneities due to a reorientation of the molecular submonolayer, reminiscent of a phase separation (*37*–*40*). Furthermore, experiments on planar MPcs have shown that alkali dopants typically interact with different ligand sites or the metal ion in a nonselective way, due to a lack of well-defined adsorption configurations (*30*). These previous results show that it is desired, albeit challenging, to switch the magnetic properties of SMMs by means of chemical doping in a precise, efficient, and reproducible way, which altogether sets a high demand on the efficiency of the doping process.

Here, we present the on-surface doping of a polynuclear SMM complex, in which multiple alkali dopants cooperatively bind and selectively interact with its magnetic core. The doping process leads to only one well-defined doped species and preserves the homogeneity and two-dimensional (2D) crystal packing of the SMMs. By means of high-resolution scanning tunneling microscopy (STM), x-ray absorption spectroscopy (XAS), and density functional theory (DFT) calculations, we show that the binding of Li atoms to the SMM not only substantially alters its intramolecular magnetic coupling but also has a huge impact on its magnetic anisotropy. The SMM of choice is $[Fe_4(L)_2(dpm)_6]$ [where H_3L = R-C$(CH_2OH)_3$ is called tripodal ligand and Hdpm = dipivaloylmethane], referred to as Fe_4, which represents one of the best-studied, prototypical SMMs (*41*). Its core comprises four high-spin d^5 Fe^{3+} ions, with three of them placed at the vertices of an equilateral triangle and enclosing another one at the center. The three peripheral ions (Fe_p) are antiferromagnetically coupled with the central one (Fe_c), giving rise to an

[1]Department of Physics, University of Konstanz, Konstanz 78457, Germany. [2]Department of Chemistry "Ugo Schiff" and INSTM Research Unit, University of Florence, Florence 50019, Italy. [3]Swiss Light Source, Paul Scherrer Institute, Villigen 5232, Switzerland. [4]Department of Chemistry, University of Konstanz, Konstanz 78457, Germany.
*Corresponding author. Email: fabian.paschke@uni-konstanz.de (F.P.); matteo.briganti@unifi.it (M.B.); federico.totti@unifi.it (F.T.); mikhail.fonin@uni-konstanz.de (M.F.)
†These authors contributed equally to this work.

$S = 5$ spin ground state (*42*). The bulky ligand shell induces an out-of-plane magnetic anisotropy that is robust against adsorption on metal, superconducting, and insulating surfaces (*7*, *43*–*51*). The derivative used in this study—Fe_4H—has R = H and is explicitly designed to favor a uniform flat adsorption geometry on surfaces (*48*, *49*, *52*, *53*), an important requirement to attain the local resolution needed to reveal details of the doping process in STM experiments (*30*).

RESULTS

Cooperative incorporation of Li into Fe_4H complexes

Well-ordered Fe_4H islands on a Pb(111) surface were obtained by the electrospray deposition method (*52*), while doping was performed by in situ Li evaporation onto the sample (see Materials and Methods). Figure 1A shows an STM image of Fe_4H complexes after co-deposition of Li. The flat-lying molecules are arranged in a bulk-like hexagonal pattern (*52*), where undoped complexes can be identified by their roughly six-pointed-star shape reflecting the six dpm ligands (*48*) (left half of Fig. 1A and fig. S1). Along with the undoped species, we observe spherical protrusions, which constitute the same hexagonal molecular lattice. The latter species appear only after Li deposition and represent Fe_4H after spontaneous attachment of n Li atoms, named $Fe_4H\text{-}Li_n$.

To discriminate the electronic structure of both complexes, we recorded differential conductance (dI/dV) spectra (Fig. 1B). Undoped Fe_4H exhibits pronounced conductance peaks at -3.1 ± 0.1 eV (referred to as "−1") and $+1.4 \pm 0.1$ eV ("+1"). They reflect elastic tunneling into multiple close-lying highest occupied and lowest unoccupied molecular orbitals of Fe_4H, respectively (*48*, *52*).

The dI/dV spectra of $Fe_4H\text{-}Li_n$ substantially differ from the ones obtained on the undoped compound. Distinct resonances are numbered as introduced above, followed by the superscript "*." While "+1*" lies at $+1.9 \pm 0.2$ eV, two clearly separated peaks appear within the transport gap of Fe_4H below the Fermi level (E_F, $V = 0$ V). These prominent resonances are persistently observed on all sphere-shaped molecules at energies of -1.1 ± 0.2 eV ("−1*") and -2.3 ± 0.1 eV ("−2*"). See section S2 for scanning tunneling spectroscopy (STS) statistics and corresponding discussion.

For the interpretation of STM data and dI/dV spectra, we carried out periodic density functional theory (pDFT) calculations to model Fe_4H on a Pb(111) surface as well as $Fe_4H\text{-}Li_n$/Pb(111) containing $n = \{1,2,3\}$ Li atoms (see Materials and Methods for computational details). Apart from the undoped SMM (fig. S1), the geometric relaxation of $Fe_4H\text{-}Li_n$ unexpectedly led to a pronounced energy minimum formed by the extreme case $n = 3$. In this configuration, that is, $Fe_4H\text{-}Li_3$, all three Li atoms relaxed inside the molecular cage. The corresponding pDFT optimized geometry is depicted in Fig. 1C. The Li atoms are incorporated into the three large voids, each defined by two dpm units and four alkoxide bridges, and confined to the plane of the Fe ions.

We provide theoretical support for the almost exclusive formation of $Fe_4H\text{-}Li_3$ by means of a profound pDFT survey (see Materials and Methods). Molecular configurations that we identify as key reaction intermediates are shown in Fig. 1D and fig. S3. Starting from three isolated Li atoms next to Fe_4H, the total energy gradually

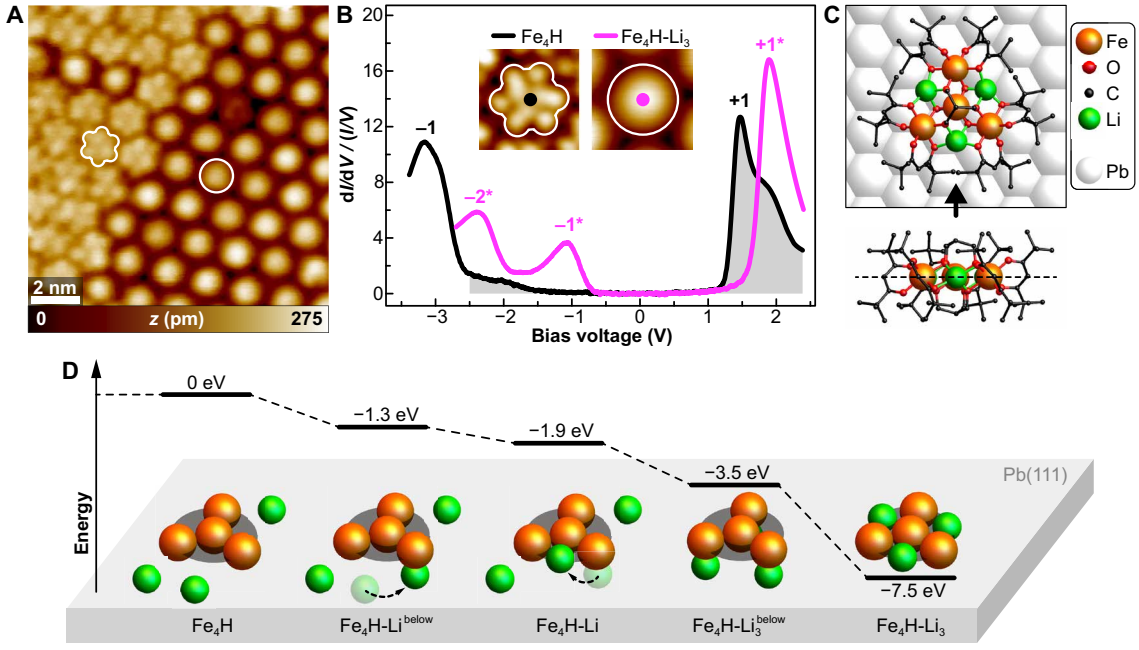

Fig. 1. Li doping of Fe_4H single-molecule magnets. (**A**) STM image of Fe_4H SMMs on Pb(111) after Li deposition. A six-lobe symmetric contour highlights an Fe_4H complex, and a circle highlights a doped $Fe_4H\text{-}Li_3$ complex. $V = +2.5$ V, $I = 20$ pA. (**B**) Normalized dI/dV spectra recorded over the center of Fe_4H and $Fe_4H\text{-}Li_3$ complexes as shown in the insets (2.1 nm by 2.1 nm). The molecular resonances are numbered as introduced in the main text. Open feedback parameters: $V = +2.5$ V, $I = 50$ pA. (**C**) pDFT relaxed geometry of $Fe_4H\text{-}Li_3$ on Pb(111). H atoms are omitted for clarity. Top: View from the top (1.8 nm by 1.6 nm). Bottom: View from the side (arrow in the top image). A dashed line indicates the plane of the four Fe and three Li atoms. (**D**) pDFT calculated total energies of the Li incorporation reaction pathway. From left to right: Fe_4H and three isolated Li ions on Pb(111), $Fe_4H\text{-}Li^{below}$ + 2 Li, $Fe_4H\text{-}Li$ + 2 Li, $Fe_4H\text{-}Li_3^{below}$, and the final configuration $Fe_4H\text{-}Li_3$. Dashed arrows indicate the trajectory of Li during optimization. See fig. S3 and Materials and Methods for more details about the process.

decreases upon their stepwise incorporation into the molecule. We observe a first energy reduction if one surface-adsorbed Li atom is placed below a peripheral Fe ion. The subsequent optimization leads to an uptake of Li toward Fe_4H, resulting in a relative minimum at which Li is coordinated by two oxygen ions—$Fe_4H\text{-}Li^{below}$. In a following step, we slightly displace the Li atom toward the alkoxide oxygen bridges, while keeping it below the plane of the Fe ions. The subsequent optimization converges to a state at which Li is incorporated in the molecular void defined by four O atoms (two from different dpm ligands and one from each tripodal ligand)—$Fe_4H\text{-}Li$. In rare cases, these intermediate states are stabilized within molecular islands and can be identified in STM (fig. S4). The total energy decreases further when three Li atoms are placed below the peripheral Fe ions—$Fe_4H\text{-}Li_3^{below}$. A last optimization step reveals that this state can easily relax, e.g., induced by thermal fluctuations, into the configuration at which all Li atoms are incorporated into the voids, that is, forming $Fe_4H\text{-}Li_3$. The pronounced energy minimum with three incorporated Li atoms suggests a strong positive binding cooperativity; that is, binding of $n = 3$ Li atoms is strongly favored compared to the cases with $n = 1$ and $n = 2$. A total energy reduction of −7.5 eV suggests that the incorporation of Li is thermodynamically favored even at room temperature. Because we explicitly observe only two stable configurations, both in experiment and in pDFT modeling, we suggest that $Fe_4H\text{-}Li_3$ is the species observed in STM images next to Fe_4H, which we corroborate in the following.

Figure 2A displays the calculated total density of states (TDOS) of Fe_4H and $Fe_4H\text{-}Li_3$ on Pb(111), projected onto the molecular states. Both curves exhibit a pronounced gap around E_F, where a small contribution originates from the terminating hydrogen on the tripodal ligand, which is pointing toward the surface. Besides the gap size, the TDOS well resembles the overall spectral shape of the dI/dV spectra (Fig. 1B).

A good agreement between theory and experiment is further confirmed upon the comparison of simulated and experimental STM topographies, shown in Fig. 2 (B and C, respectively). The corresponding energies $E_{sim} < 0$ and $E_{sim} > 0$ as well as the bias voltages $V_{exp} < 0$ and $V_{exp} > 0$ include the resonances −2*, −1*, +1, and +1* (gray backgrounds in Figs. 1B and 2A). In STM images, undoped Fe_4H always exhibits the typical six-pointed-star appearance owing to the six dpm ligands of the ligand shell (*48*, *52*), with less intensity when imaged in the gap (left molecule in Fig. 2C, marked in gray). Precisely, its symmetry is threefold with a three-pointed star and three separated lobes, with the molecules' chirality (*42*) imprinted in a slight distortion of the star. $Fe_4H\text{-}Li_3$ exhibits a similar intensity distribution when imaged at $V_{exp} < 0$, confirming its structural integrity (right molecule in Fig. 2C, marked in magenta). However, upon scanning with $V_{exp} > 0$ around +1* (up to +2.5 V), $Fe_4H\text{-}Li_3$ appears as a compact threefold symmetric donut-like structure with vanishing intensity over the dpm ligands (Fig. 2C). The observed molecular shapes are well reproduced within calculated Tersoff-Hamann images based on the pDFT results (Fig. 2B; see fig. S5 for data at different bias voltages). We note that for STM tips with a more blunt tip apex, that is, with less lateral resolution (*54*), the donut-like appearance manifests itself as spherical protrusion (Fig. 1, A and B), which can be well reproduced in the simulations (fig. S5C).

Further compelling evidence for the formation of $Fe_4H\text{-}Li_3$ is obtained upon comparing frontier molecular orbitals of Fe_4H and $Fe_4H\text{-}Li_3$ to spatially resolved dI/dV resonances (see section S6). On the basis of the comparison of calculation and experiment, we furthermore exclude another possible Li addition scenario, that is, a homolytical reaction between Li and the terminating hydrogen of the tripodal ligand (section S7).

Its pronounced energetic stability along with the good agreement of experimental and calculated STM and STS signatures allow us to conclude that $Fe_4H\text{-}Li_3$ has been formed by the cooperative incorporation (*55*) of three Li atoms into Fe_4H on the Pb(111) surface.

Selective redox doping of Fe_4H

Figure 3A shows the calculated projected density of states (PDOS) of both Fe_4H and $Fe_4H\text{-}Li_3$ on Pb(111). In undoped Fe_4H, the "+1" peak is dominated by unoccupied *3d* states of the three peripheral Fe^{3+} ions. The states on the central Fe^{3+} ion (named "+2") are slightly shifted in energy and contribute to the subsequent broad peak in the TDOS. In $Fe_4H\text{-}Li_3$, the incorporation of three Li atoms causes an effective charge transfer of 1*e* toward each of the peripheral Fe ions. This leads to a lowering of the corresponding states below E_F, forming −1* in the PDOS (dashed arrow in Fig. 3A) and −1* in the dI/dV spectrum (Fig. 1B). Each Fe_p ion in $Fe_4H\text{-}Li_3$ is thus fully reduced to Fe^{2+}. The orbital occupations of the central Fe^{3+} ion do not change, but now, its orbitals appear as a frontier peak named "+1*" in the PDOS. In agreement with the shift of orbital energies, the spatial distributions of orbitals comprising

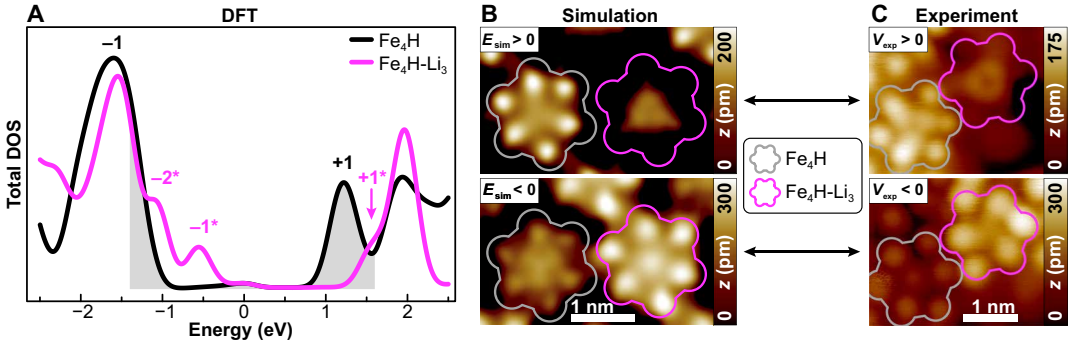

Fig. 2. Electronic structure of $Fe_4H\text{-}Li_3$. (**A**) Total DOS calculated for Fe_4H and $Fe_4H\text{-}Li_3$ on Pb(111). Frontier peaks are numbered according to the main text and Fig. 1B. (**B**) Simulated STM topographic images calculated at the energies $E_{sim} = +1.6$ eV (top) and $E_{sim} = -1.4$ eV (bottom) [gray background in (A)]. Molecular shapes around Fe_4H (gray) and $Fe_4H\text{-}Li_3$ (magenta) are sketched as a guide to the eye. (**C**) STM images recorded at bias voltages $V_{exp} = +2.5$ V (top) and $V_{exp} = -2.5$ V (bottom) (gray background in Fig. 1B). $I_{-2.5V} = 10$ pA, $I_{+2.5V} = 40$ pA.

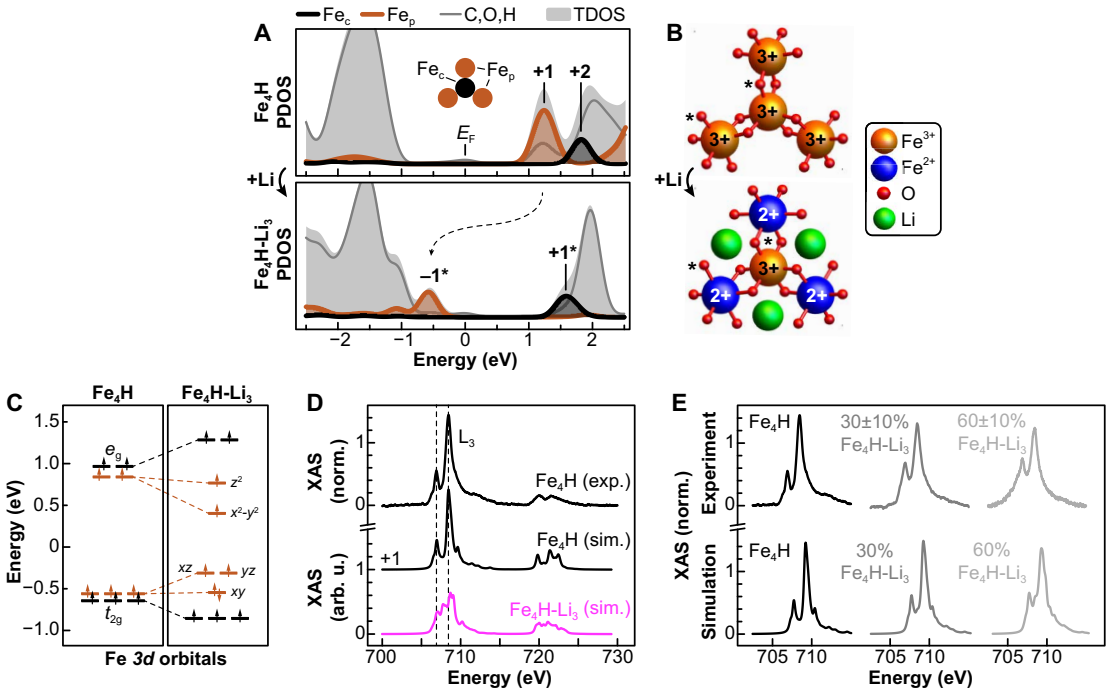

Fig. 3. Selective redox doping of Fe_4H-Li_3. (**A**) Calculated PDOS of Fe_4H (top) and Fe_4H-Li_3 (bottom) on Pb(111). Inset: Schematic of the Fe_4 core composed of central Fe_c and peripheral Fe_p ions. The PDOS is evaluated for Fe_c (black), the Fe_p ions (orange), and combined on the remaining atoms (gray). Shaded areas show the TDOS (Fig. 2A). (**B**) Calculated geometries of the oxygen-coordinated Fe ions in Fe_4H (top) and Fe_4H-Li_3 (bottom). Fe^{3+} and Fe^{2+} ions are colored orange and blue, respectively. (**C**) Change of the 3*d* crystal field splittings and occupations at the Fe ions upon Li doping. The color code for $Fe_{c/p}$ is the same as in (A). (**D**) Top: Measured XAS spectrum on Fe_4H/Pb(111). Center and bottom: Simulated XAS spectra of Fe_4H (black, 4 × Fe^{3+}) and Fe_4H-Li_3 (magenta, 1 × Fe^{3+} and 3 × Fe^{2+}). Dashed lines denote the split L_3 peak. (**E**) Top: Evolution of measured XAS spectra upon growing relative amount of Fe_4H-Li_3 (from left to right). Bottom: Simulated XAS spectra for 0, 30, and 60% of Fe_4H-Li_3 in an otherwise undoped ensemble of Fe_4H. Measurement parameters for XAS spectra: $B = 6.8$ T, $\theta = 0°$, and $T = 3$ K.

−1* and +1* well resemble the ones of +1 and +2, respectively (fig. S6). While orbitals comprising +1 are localized at the Fe_p ions with contributions on the outer (dpm) ligands, orbitals comprising "+1*" are localized at the central Fe ion and have contributions only on the central (tripodal) ligands. These spatial differences between the frontier orbitals explain the different STM appearances of Fe_4H and Fe_4H-Li_3 at $V_{exp} > 0$ (Fig. 2C). Because tunneling at voltages around the frontier resonance energy is dominated by transport through the frontier orbitals and thus resembles their spatial distribution, undoped Fe_4H is imaged with intensity over the outer ligands (resembling +1), while doped Fe_4H-Li_3 is imaged with intensity only over the central ligand (resembling +1*, see section S6 for details). Summarizing, we thus observe a doping-induced reduction from Fe^{3+} to Fe^{2+} of the peripheral iron ions, schematically depicted in Fig. 3B. The resulting mixed-valence compound (*56*) Fe_4H-Li_3 may therefore be referred to as doped Fe_4H SMM.

The incorporation of three Li atoms induces distortions on the coordination geometry of all Fe ions, which becomes apparent in a slight positional change of the alkoxide and ketoenolate bridges (marked by asterisks for a single Li pocket in Fig. 3B). In undoped Fe_4H, all Fe ions reside in an octahedral crystal field slightly distorted toward a trigonal antiprism (*42*) that leads to well separated t_{2g} and e_g orbitals in the pDFT calculation (Fig. 3C). The mean crystal field splitting parameter amounts to $10Dq \approx 1.5$ eV, close to values observed in other Fe_4 derivatives, both on surfaces and in the gas phase (*42*–*45*). On the central Fe^{3+} ion in Fe_4H-Li_3, $10Dq$ increases by 40% while keeping the octahedral environment intact. This changes for the peripheral iron ions, where the switch to Fe^{2+} is accompanied by an asymmetric expansion of the Fe_p-O distances to the oxygen ions that are involved in the coordination of Li^+. Such a blossom-like expansion stabilizes the $d_{x^2-y^2}$ and d_{xy} orbitals with respect to d_{z^2} and d_{xz}/d_{yz}, respectively (Fig. 3C; for the local reference frame of Fe_p, see fig. S8). The splitting of Fe_p^{2+} can be mimicked by a local D_{4h} symmetry, and corresponding values of *Dq*, *Dt*, and *Ds* are listed in table S1.

To experimentally access the electronic state of the doped complex, we use synchrotron-based XAS and x-ray magnetic circular dichroism (XMCD) experiments (*43*, *57*). The top curve in Fig. 3D shows an XAS spectrum recorded on an undoped submonolayer of Fe_4H on Pb(111). The spectral features are in perfect agreement with previously reported results for surface-adsorbed Fe_4H (*48*, *53*) and other Fe_4 derivatives (*7*, *43*–*47*, *50*, *51*), and imply an intact $S = 5$ spin ground state that originates from a ferrimagnetic spin alignment between the spins of the Fe_c and Fe_p ions (see section S9 for further data and discussion). The experimental curve can be well reproduced by simulating the XAS spectrum of a pure Fe_4H sample (central curve in Fig. 3D). Artificially increasing the amount of Fe^{2+} and using the pDFT calculated crystal field parameters to model the XAS signature of doped Fe_4H-Li_3 results in a strongly reduced L_3 subpeak ratio along with the emergence of an intermediate peak (bottom curve in Fig. 3D). The XAS spectrum of a mixed submonolayer of Fe_4H and Fe_4H-Li_3 will show a superposition of these two curves, with its L_3 subpeak ratio being a reasonable measure for the amount of Fe_4H-Li_3 complexes in the sample (see section S10 for computational details).

Using STM and by counting doped complexes on a large number of molecular islands, we determine relative amounts of Fe_4H-Li_3 for different amounts of co-deposited Li (section S11). For low amounts of Li that correspond to ≤60% of Fe_4H-Li_3 in the sample, only few molecular fragments can be found on the surface, and molecular islands remain widely intact (fig. S11). For larger amounts of Li, we observe substantial molecular fragmentation, in contrast to experiments on single-ion complexes carried out at the saturation limit (*32*). This allows us to record a series of XAS spectra with relative amounts of 0%, 30 ± 10%, and 60 ± 10% of Fe_4H-Li_3 in the submonolayer (top curves in Fig. 3E). Along with the growing relative amount of Fe_4H-Li_3, we detect a gradually increasing subpeak ratio of 0.4 → 0.5 → 0.6, a slight broadening at the curve's base, and a decreasing depth of the dip in between the two L_3 peaks. The spectral evolution can be well reproduced by a linear superposition of the calculated XAS spectra of Fe_4H and doped Fe_4H-Li_3 (Fig. 3D) if we assume 0, 30, and 60% of all molecules to be doped with three Li atoms (lower curves in Fig. 3E). We thus conclude that the observed oxidation state change reflects the increasing number of Fe_4H-Li_3 complexes in the sample, with each consisting of one Fe^{3+} and three Fe^{2+} ions as suggested by the previous STM/pDFT analysis.

Switch of the single-molecule magnetism upon Li doping

The impact of threefold Li doping on its electronic structure comes along with profound implications on the molecular magnetism of the Fe_4H SMM. In Fe_4 SMMs, the four Fe^{3+} ions ($S = \frac{5}{2}$) interact via superexchange (J) mediated by the alkoxide bridges (Fig. 4A) (*42*). Its magnetic ground state can be well described by two antiferromagnetic coupling constants $J > 0$: a dominant one acting between the three peripheral and the central iron spins (J_1) and a substantially smaller one connecting the peripheral iron spins (J_2). This renders a total spin ground state of $S = 5$ in pristine Fe_4H and related Fe_4-based derivatives (*41*, *52*), which has been shown to be widely robust upon surface adsorption (*7*, *25*, *48*, *50*) and incorporation into three-terminal devices (*27*).

Our pDFT calculation of Fe_4H/Pb(111) corroborates these findings and reveals an increase of J_1 of 35%, driven by a combination of a growing Fe_p-O-Fe_c angle (102.86° → 103.85°) and a decreasing γ pitch (*25*, *58*, *59*) upon surface relaxation. The degeneracy of the spin ground state manifold is lifted by the molecular ligand shell, modeled to first order using the effective spin Hamiltonian (*60*) $\hat{H}_{ZFS} = D\hat{S}_z^2$. D denotes the magnetic anisotropy and is essential for the definition of SMMs. Its sign determines a magnetic easy-axis ($D < 0$) or easy-plane ($D > 0$) behavior. For Fe_4H/Pb(111), we calculate $D_{DFT} = -0.32\ cm^{-1}$ with a magnetic easy-axis pointing orthogonal to the plane of the four iron atoms (top panel in Fig. 4B). This denotes a slight reduction with respect to the bulk value (*52*), caused by structural relaxation of the Fe_2O_2 helical pitch (*61*), and can be assessed experimentally by means of an XMCD experiment (*62*). The top panel in Fig. 4C shows magnetization curves measured on an undoped sample with the magnetic field applied in two directions (see Materials and Methods for details). A larger magnetic moment in the out-of-plane direction as compared to grazing angle indicates a net magnetic easy-axis along the surface normal. In combination with the uniformly flat-lying adsorption configuration observed in STM, we suggest that this holds for every complex on the sample as observed on other surfaces (*48*, *53*). Fitting the XMCD curves to $D\hat{S}_z^2 + g\mu_B\mathbf{B}\hat{\mathbf{S}}$ and using $S = 5$ reveals a magnetic anisotropy of $D_{exp} = -0.39 \pm 0.03\ cm^{-1}$, which reflects a slight absolute reduction compared to the bulk value (*52*) in line with the pDFT prediction. This finding confirms the robust nature of the magnetic core of Fe_4H upon adsorption on metal surfaces (*63*).

The reduction of the Fe_p ions upon Li attachment results in a respective spin state change to $S_p^* = 2$ (Fig. 4A). Keeping the exchange interactions unaltered would thus result in a $S^* = 7/2$ spin ground state of Fe_4H-Li_3. Our pDFT survey suggests two major changes of the molecular magnetism in the Fe_4H-Li_3 complex. First, the dominant exchange coupling J_1^* not only decreases upon Li incorporation, but also switches its sign from an antiferro- to a ferromagnetic interaction ($J_1^* < 0$) (see Fig. 4A). The antiferromagnetic next-nearest

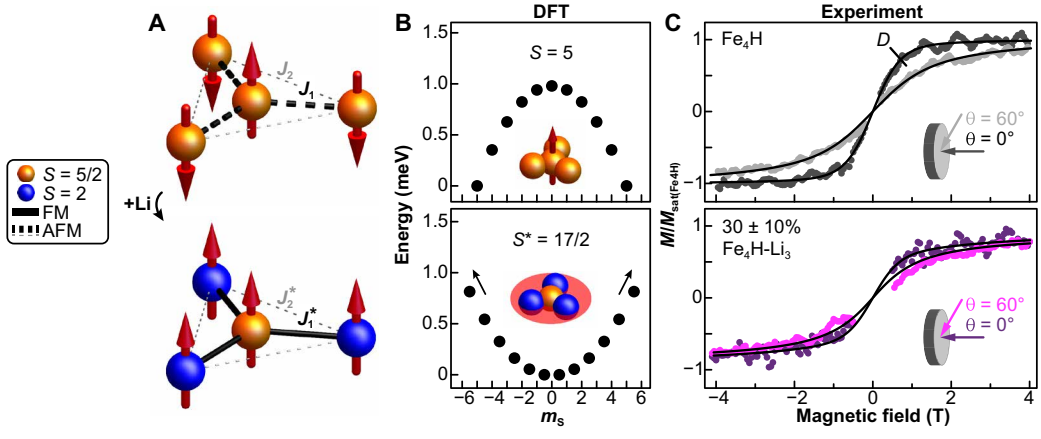

Fig. 4. Evolution of magnetic properties of Fe_4H upon Li doping. (**A**) Coupling scheme of the four Fe spins in Fe_4H (top) and Fe_4H-Li_3 (bottom). Ferromagnetic (FM) and antiferromagnetic (AFM) exchange interactions $J_{1,2}^{(*)}$ are sketched as solid and dashed lines, respectively. Thick (thin) lines denote a large (small) exchange magnitude. (**B**) pDFT calculated zero-field splitting of the spin ground states of Fe_4H (top) and Fe_4H-Li_3 (bottom). Arrows indicate further states above 1 meV outside the diagram. Insets visualize out-of-plane (red arrow) and in-plane (red disk) magnetic anisotropy. (**C**) XMCD magnetization curves (data points) obtained on undoped Fe_4H/Pb(111) (top) and a partially doped sample with roughly 30 ± 10% of Fe_4H-Li_3 complexes (bottom). $T = 3$ K, $dB/dt = 2$ T/min. Solid lines in the top panel denote a fit to $D\hat{S}_z^2 + g\mu_B\mathbf{B}\hat{\mathbf{S}}$. Solid lines in the bottom panel refer to a simulation using the fitted D for Fe_4H, the calculated D^* and S^* for Fe_4H-Li_3, and an amount of 30% of Fe_4H-Li_3 in an otherwise undoped ensemble of Fe_4H. See fig. S12 for simulated curves at 60 and 100% of Fe_4H-Li_3.

neighbors interaction, J_2^*, stays roughly unaltered, as can be seen in Table 1. As reported previously (*58*, *64*), sign and magnitude of the exchange constants strongly depend on the Fe_p-O-Fe_c angle. In our optimized geometries, this angle changes from 103.85° in Fe_4H to 99.37° in Fe_4H-Li_3. For Fe^{2+}-Fe^{3+} dimers, angles above 100° favor an antiferromagnetic interaction, while a ferromagnetic exchange was predicted for angles below roughly 100° (*65*, *66*). Furthermore, the mixed-valence nature of Fe_4H-Li_3 renders the total magnetic behavior a superposition of exchange and double exchange interactions, of which the latter are always ferromagnetic (*65*, *67*). Both the decreasing Fe_p-O-Fe_c angle as well as the oxidation state change thus favor an overall ferromagnetic behavior for Fe_4H-Li_3, which explains the observed inversion.

Second, the pDFT results suggest the magnetic anisotropy to evolve from an easy-axis to an easy-plane configuration expressed by $D^* > 0$ along with an absolute decrease of around 30% with respect to D of undoped Fe_4H (see Table 1 and Fig. 4B). The change is driven by a variation of the local anisotropies of the Fe_p ions, which change from an easy-axis to an easy-plane type magnetic anisotropy (values are collected in table S2). This gets as well apparent from the change of the overall spatial orientation of the *3d* orbitals of Fe_p (fig. S6). For Fe_c, no substantial orbital changes are observed upon Li doping.

Figure S12 displays simulated magnetization curves for different relative amounts of Fe_4H-Li_3 in a sample of Fe_4H. The sign switch of D results in a reduction of the total magnetic anisotropy in mixed submonolayers of Fe_4H and Fe_4H-Li_3, followed by a reversal of out-of-plane and in-plane magnetization magnitudes in $M(B)$ in a fully doped sample. While the latter cannot be realized in our experiment due to substantial molecular defragmentation, we acquire XMCD magnetization curves on a sample with 30 ± 10% of Fe_4H-Li_3 complexes in an otherwise undoped submonolayer (see bottom panel in Fig. 4C). The saturation magnitude decreases due to a reduced XMCD signal of Fe_4H-Li_3 at the L_3 edge (figs. S9 and S12) and the area between the two curves is substantially smaller compared to the measurement on the undoped sample. This finding is in good agreement with the simulation that assumes 30% of Fe_4H-Li_3 in the sample (solid lines in Fig. 4C; see also fig. S12), supporting a reduction of the total magnetic anisotropy.

DISCUSSION

The cooperative (or allosteric) binding (*55*) of three Li atoms to Fe_4H, via less stable intermediates, is particularly remarkable. A simultaneous inclusion of two or more guest molecules to a multitopic host was found to be involved in efficient catalytic transformations (*68*), in host-guest chemistry (*69*, *70*), and in transport processes like oxygen transport by the Heme system (*71*). However, cooperative binding of more than one metal ion into available pockets of a polynuclear metal complex has been rarely reported (*72*), and its characterization on a single-molecule level has remained elusive. In our study, cooperative Li inclusion selectively reduces all peripheral Fe^{3+} ions to Fe^{2+}, which demonstrates chemical redox doping of a polynuclear SMM. The process preserves the 2D crystal packing and we do not observe phase separations as reported for C_{60} experiments (*36*–*40*). It induces only small modifications on the molecular geometry, but with substantial changes on the single-molecule magnetism of Fe_4H. The intramolecular exchange interaction between the iron spins switches from an antiferro- to a ferromagnetic coupling and the magnetic anisotropy from an easy-axis to an easy-plane configuration.

Previous attempts targeting the manipulation of magnetic properties in polynuclear SMMs on the one hand focused on gate-induced doping of Fe_4 complexes in break-junction experiments. For both oxidation and reduction of Fe_4, they revealed a slight enhancement of D (*27*, *73*), and respective DFT calculations suggested a spin ground state of $S = \frac{9}{2}$ for both cases (*74*). On the other hand, the Fe_p-O-Fe_c angle in Fe_4 could reversibly be compressed by an STM tip, leading to a temporal increase of the intramolecular exchange interaction (*25*). In stark contrast, and not limited to Fe_4 complexes, our results propose chemical redox doping as an efficient tool for a univocal and selective manipulation of both oxidation and spin states in specifically tailored SMM complexes. For example, synthetic strategies can take single ion reactivities into account, or target a positive binding cooperativity that then allows for efficient self-driven, multiple alkali doping.

We emphasize that the manipulation of the electronic and magnetic structure in Fe_4H-Li_3 so far is of permanent nature, as a consequence of the large energy stabilization when Li is incorporated into the Fe_4 skeleton. In our experiments, the application of voltage pulses did not induce any changes up to voltage values at which the molecules deteriorate. A stable binding of the Li ions into three equivalent adsorption sites stays in sharp contrast to previous experiments performed on single-ion MPcs (*30*, *32*), in which dopants can switch between multiple different interaction sites due to the planar molecular geometry (*32*, *75*). The character of an effective atom trap could be interesting for molecular sensing applications or magnetic switches that rely on magnetic readout. In this regard,

Table 1. Magnetic properties of Fe_4H and Fe_4H-Li_3. $J > 0$ and $J < 0$ describe an antiferro- and ferromagnetic exchange interaction, respectively. E denotes the transversal term in the effective spin Hamiltonian (*60*). The total anisotropies D were calculated from single-ion anisotropy tensors (corresponding D values in table S2) and projection coefficients (table S4) for each Fe ion.

			This work		
		Fe_4H bulk	Fe_4H/Pb(111)		Fe_4H-Li_3/Pb(111)
		Exp. (*52*)	pDFT	Exp.	pDFT
(cm^{-1})	J_1	+16.9	+23.7 ± 1.0		−13.1 ± 2.3
	J_2	+0.95	+1.60		+1.97
	D	−0.427	−0.316	−0.39 ± 0.03	+0.219
	E		−0.017		−0.012
	S	5	5	5	17/2

further investigations of the binding dynamics, i.e., by supplying Li at low temperatures and doping of different Fe_4 derivatives or other polynuclear SMMs, are of particular interest. The permanent nature of the doping could also be altered by exploring larger alkali metals, e.g., Na or Cs atoms. A combination with in-depth magnetic studies using STM (*25*, *33*, *49*), XMCD (*50*), or Mössbauer spectroscopy (*76*) could provide guiding principles for synthetic procedures that tailor the reactivity of molecular binding sites like the molecular voids in Fe_4H.

Follow-up studies on Fe_4H-Li_3 might encompass the local investigation of its inter-multiplet spin state transitions and magnetic anisotropy (*25*, *49*) using the spectral resolution and spin sensitivity of a superconducting (*33*) or a functionalized STM tip (*77*), respectively. Driving low-energy intra-multiplet transitions would allow to track the switch of the magnetic anisotropy upon doping, and ESR-based measurement schemes are expected to distinguish the ground states m_s of neutral and doped species (*78*).

Our work pictures an unusual result of an exceptional well-defined local manipulation of molecular magnetism. This is achieved by cooperative and highly selective chemical redox doping of one of the most archetypal SMMs. The results propose atomic doping as a feasible way to controllably switch the properties of polynuclear magnetic complexes that comprise bulky and functional ligand groups.

MATERIALS AND METHODS

STM experiments

Samples were prepared in situ for all experiments. The Pb(111) single crystal (Surface Preparation Laboratory B. V.) was cleaned by repeated cycles of Ar^+ sputtering at 1.5 kV and annealing in ultra-high-vacuum (UHV) up to 215°C. Electrospray deposition of Fe_4H was performed as described elsewhere (*52*, *79*, *80*). Li deposition was performed by thermal evaporation from alkali metal dispensers (SAES Getters), while the sample was held at room temperature. The deposition rate was determined using a quartz microbalance calibrated by STM. Further details about the preparation can be found in section S13.

STM and STS experiments were performed in a two-chamber UHV system (base pressure 5×10^{-11} mbar), equipped with an Omicron Cryogenic-STM. The STM was operated at temperatures of 2 to 5 K. All STM measurements were carried out in the constant-current mode using grinded and polished PtIr tips (Nanoscore GmbH). The sign of the bias voltage V corresponds to the potential applied to the sample so that $V > 0$ denotes tunneling into unoccupied states of the sample. $I(V)$ spectra were numerically differentiated and normalized to the I/V signal (*81*). The BCS gap of Pb(111) (around 1.2 meV) is not resolved in the dI/dV spectra because of the large measurement range ($V = \pm 2.5$ V), which implies that the tunneling current around E_F is too small to generate a measurable dI/dV signal. The amount of doped Fe_4H-Li_3 complexes for each Li coverage was estimated by counting molecules on a large number of molecular islands of varying sizes and shapes (see section S11 for more details).

XAS/XMCD

XAS and XMCD experiments were performed at the X-Treme beamline (*82*) of the Swiss Light Source at the Paul Scherrer Institute. The XAS signal was acquired in the total electron yield mode, with an applied magnetic field B being aligned antiparallel to the x-ray beam and forming an angle θ with respect to the sample surface normal. We used a defocused x-ray beam to minimize the photon flux. Accordingly, no substantial beam damage has been observed in the spectra throughout the measurements. XAS spectra were recorded at the Fe $L_{2,3}$ edges and normalized to their average L_3 peaks' intensities. The XAS was calculated as $(\sigma_+ + \sigma_-)$, and the XMCD was calculated as $(\sigma_+ - \sigma_-) / (\sigma_+ + \sigma_-)$, where σ_+ and σ_- denote the XAS signals obtained with left- and right-hand circularly polarized light, respectively. Magnetization curves were acquired by tracking XMCD(B) at the L_3 edge (708.5 eV). XAS and XMCD data acquired before each magnetization curve are shown in fig. S9. Simulation details of XAS/XMCD spectra and magnetization curves can be found in sections S10 and S12, respectively.

Computational details

The CP2K 6.1 quantum chemistry software (*83*) was used for all pDFT calculations. The RevPBE functional (*84*, *85*), along with rVV10 empirical dispersion corrections (*86*), were used in all simulations. Norm-conserving Goedecker-Teter-Hutter pseudopotentials (*87*) and double zeta basis sets with polarization functions (DZVP-MOLOPT-SR) were used for all atoms. The cell parameters were kept fixed throughout the optimizations. The plane-wave cutoff value was set to 400 Ry. The wave function convergence threshold (EPS_SCF) was set to 1.0×10^{-6} Hartree, while the maximum force for the geometry optimization was set to $4.5 \times 10^{-3}\ a_0^{-1}$ Hartree, where a_0 is the Bohr radius. A self-consistent field (SCF) diagonalization method was applied, which adds an electron smearing of the molecular orbital occupation numbers with a Fermi-Dirac distribution at 1500 K. The energies of the potential energy surface landscape were obtained by performing an orbital transformational SCF on the optimized geometries. Further details can be found in section S14.

Supplementary Materials

This PDF file includes:

Figs. S1 to S14
Tables S1 to S4
References

REFERENCES AND NOTES

1. C. Joachim, J. K. Gimzewski, A. Aviram, Electronics using hybrid-molecular and mono-molecular devices. *Nature* **408**, 541–548 (2000).
2. S. Jan van der Molen, P. Liljeroth, Charge transport through molecular switches. *J. Phys. Condens. Matter* **22**, 133001 (2010).
3. K. Morgenstern, Switching individual molecules by light and electrons: From isomerisation to chirality flip. *Prog. Surf. Sci.* **86**, 115–161 (2011).
4. T. Miyamachi, M. Gruber, V. Davesne, M. Bowen, S. Boukari, L. Joly, F. Scheurer, G. Rogez, T. K. Yamada, P. Ohresser, E. Beaurepaire, W. Wulfhekel, Robust spin crossover and memristance across a single molecule. *Nat. Commun.* **3**, 938 (2012).
5. J. L. Zhang, J. Q. Zhong, J. D. Lin, W. P. Hu, K. Wu, G. Q. Xu, A. T. S. Wee, W. Chen, Towards single molecule switches. *Chem. Soc. Rev.* **44**, 2998–3022 (2015).
6. D. Xiang, X. Wang, C. Jia, T. Lee, X. Guo, Molecular-scale electronics: From concept to function. *Chem. Rev.* **116**, 4318–4440 (2016).
7. M. Mannini, F. Pineider, P. Sainctavit, C. Danieli, E. Otero, C. Sciancalepore, A. M. Talarico, M.-A. Arrio, A. Cornia, D. Gatteschi, R. Sessoli, Magnetic memory of a single-molecule quantum magnet wired to a gold surface. *Nat. Mater.* **8**, 194–197 (2009).
8. S. Sanvito, Molecular spintronics. *Chem. Soc. Rev.* **40**, 3336 (2011).
9. H. Tanaka, M. Akai-Kasaya, A. TermehYousefi, L. Hong, L. Fu, H. Tamukoh, D. Tanaka, T. Asai, T. Ogawa, A molecular neuromorphic network device consisting of single-walled carbon nanotubes complexed with polyoxometalate. *Nat. Commun.* **9**, 2693 (2018).
10. F. Moresco, G. Meyer, K. H. Rieder, H. Tang, A. Gourdon, C. Joachim, Conformational changes of single molecules induced by scanning tunneling microscopy manipulation: A route to molecular switching. *Phys. Rev. Lett.* **86**, 672–675 (2001).
11. M. Alemani, M. V. Peters, S. Hecht, K. H. Rieder, F. Moresco, L. Grill, Electric field-induced isomerization of azobenzene by STM. *J. Am. Chem. Soc.* **128**, 14446–14447 (2006).

12. P. Liljeroth, J. Repp, G. Meyer, Current-induced hydrogen tautomerization and conductance switching of naphthalocyanine molecules. *Science* **317**, 1203–1206 (2007).
13. S. Y. Quek, M. Kamenetska, M. L. Steigerwald, H. J. Choi, S. G. Louie, M. S. Hybertsen, J. B. Neaton, L. Venkataraman, Mechanically controlled binary conductance switching of a single-molecule junction. *Nat. Nanotechnol.* **4**, 230–234 (2009).
14. T. Komeda, H. Isshiki, J. Liu, Y. F. Zhang, N. Lorente, K. Katoh, B. K. Breedlove, M. Yamashita, Observation and electric current control of a local spin in a single-molecule magnet. *Nat. Commun.* **2**, 217 (2011).
15. J. Wirth, N. Hatter, R. Drost, T. R. Umbach, S. Barja, M. Zastrow, K. Rück-Braun, J. I. Pascual, P. Saalfrank, K. J. Franke, Diarylethene molecules on a Ag(111) surface: Stability and electron-induced switching. *J. Phys. Chem. C* **119**, 4874–4883 (2015).
16. L. Gerhard, K. Edelmann, J. Homberg, M. Valášek, S. G. Bahoosh, M. Lukas, F. Pauly, M. Mayor, W. Wulfhekel, An electrically actuated molecular toggle switch. *Nat. Commun.* **8**, 14672 (2017).
17. G. Ke, C. Duan, F. Huang, X. Guo, Electrical and spin switches in single-molecule junctions. *InfoMat* **2**, 92–112 (2020).
18. M.-H. Jo, J. E. Grose, K. Baheti, M. M. Deshmukh, J. J. Sokol, E. M. Rumberger, D. N. Hendrickson, J. R. Long, H. Park, D. C. Ralph, Signatures of molecular magnetism in single-molecule transport spectroscopy. *Nano Lett.* **6**, 2014–2020 (2006).
19. A. Ardavan, O. Rival, J. J. L. Morton, S. J. Blundell, A. M. Tyryshkin, G. A. Timco, R. E. P. Winpenny, Will spin-relaxation times in molecular magnets permit quantum information processing? *Phys. Rev. Lett.* **98**, 057201 (2007).
20. L. Bogani, W. Wernsdorfer, Molecular spintronics using single-molecule magnets. *Nat. Mater.* **7**, 179–186 (2008).
21. M. Urdampilleta, N. V. Nguyen, J. P. Cleuziou, S. Klyatskaya, M. Ruben, W. Wernsdorfer, Molecular quantum spintronics: Supramolecular spin valves based on single-molecule magnets and carbon nanotubes. *Int. J. Mol. Sci.* **12**, 6656–6667 (2011).
22. E. Moreno-Pineda, W. Wernsdorfer, Measuring molecular magnets for quantum technologies. *Nat. Rev. Phys.* **3**, 645–659 (2021).
23. S. Chicco, G. Allodi, A. Chiesa, E. Garlatti, C. D. Buch, P. Santini, R. de Renzi, S. Piligkos, S. Carretta, Proof-of-concept quantum simulator based on molecular spin qudits. *J. Am. Chem. Soc.* **146**, 1053–1061 (2024).
24. A. Cornia, A. C. Fabretti, M. Pacchioni, L. Zobbi, D. Bonacchi, A. Caneschi, D. Gatteschi, R. Biagi, U. D. Pennino, V. De Renzi, L. Gurevich, H. S. J. Van der Zant, Direct observation of single-molecule magnets organized on gold surfaces. *Angew. Chemie Int. Ed. Engl.* **42**, 1645–1648 (2003).
25. J. A. Burgess, L. Malavolti, V. Lanzilotto, M. Mannini, S. Yan, S. Ninova, F. Totti, S. Rolf-Pissarczyk, A. Cornia, R. Sessoli, S. Loth, Magnetic fingerprint of individual Fe_4 molecular magnets under compression by a scanning tunnelling microscope. *Nat. Commun.* **6**, 8216 (2015).
26. S. Thiele, F. Balestro, R. Ballou, S. Klyatskaya, M. Ruben, W. Wernsdorfer, Electrically driven nuclear spin resonance in single-molecule magnets. *Science* **344**, 1135–1138 (2014).
27. E. Burzurí, R. Gaudenzi, H. S. J. van der Zant, Observing magnetic anisotropy in electronic transport through individual single-molecule magnets. *J. Phys. Condens. Matter* **27**, 113202 (2015).
28. R. Robles, N. Lorente, H. Isshiki, J. Liu, K. Katoh, B. K. Breedlove, M. Yamashita, T. Komeda, Spin doping of individual molecules by using single-atom manipulation. *Nano Lett.* **12**, 3609–3612 (2012).
29. A. Mugarza, R. Robles, C. Krull, R. Korytár, N. Lorente, P. Gambardella, Electronic and magnetic properties of molecule-metal interfaces: Transition-metal phthalocyanines adsorbed on Ag(100). *Phys. Rev. B* **85**, 155437 (2012).
30. C. Krull, R. Robles, A. Mugarza, P. Gambardella, Site- and orbital-dependent charge donation and spin manipulation in electron-doped metal phthalocyanines. *Nat. Mater.* **12**, 337–343 (2013).
31. L. Liu, K. Yang, Y. Jiang, B. Song, W. Xiao, L. Li, H. Zhou, Y. Wang, S. Du, M. Ouyang, W. A. Hofer, A. H. Castro Neto, H. J. Gao, Reversible single spin control of individual magnetic molecule by hydrogen atom adsorption. *Sci. Rep.* **3**, 1210 (2013).
32. S. Stepanow, A. Lodi Rizzini, C. Krull, J. Kavich, J. C. Cezar, F. Yakhou-Harris, P. M. Sheverdyaeva, P. Moras, C. Carbone, G. Ceballos, A. Mugarza, P. Gambardella, Spin tuning of electron-doped metal phthalocyanine layers. *J. Am. Chem. Soc.* **136**, 5451–5459 (2014).
33. B. W. Heinrich, L. Braun, J. I. Pascual, K. J. Franke, Tuning the magnetic anisotropy of single molecules. *Nano Lett.* **15**, 4024–4028 (2015).
34. X. Meng, J. Möller, M. Mansouri, D. Sánchez-Portal, A. Garcia-Lekue, A. Weismann, C. Li, R. Herges, R. Berndt, Controlling the spin states of FeTBrPP on Au(111). *ACS Nano* **17**, 1268–1274 (2023).
35. R. Yamachika, M. Grobis, A. Wachowiak, M. F. Crommie, Controlled atomic doping of a single C–60 molecule. *Science* **304**, 281–284 (2004).
36. A. Wachowiak, R. Yamachika, K. H. Khoo, Y. Wang, M. Grobis, D. H. Lee, S. G. Louie, M. F. Crommie, Visualization of the molecular Jahn-Teller effect in an insulating K_4C_{60} monolayer. *Science* **310**, 468–470 (2005).
37. S. Han, M.-X. Guan, C.-L. Song, Y.-L. Wang, M.-Q. Ren, S. Meng, X.-C. Ma, Q.-K. Xue, Visualizing molecular orientational ordering and electronic structure in Cs_nC_{60} fulleride films. *Phys. Rev. B* **101**, 085413 (2020).
38. A. Tamai, A. P. Seitsonen, R. Fasel, Z.-X. Shen, J. Osterwalder, T. Greber, Doping-induced reorientation of C_{60} molecules on Ag(111). *Phys. Rev. B* **72**, 085421 (2005).
39. Y. Wang, R. Yamachika, A. Wachowiak, M. Grobis, K. H. Khoo, D.-H. Lee, S. G. Louie, M. F. Crommie, Novel orientational ordering and reentrant metallicity in K_xC_{60} monolayers for $3 \leq x \leq 5$. *Phys. Rev. Lett.* **99**, 086402 (2007).
40. M. Grobis, R. Yamachika, A. Wachowiak, X. Lu, M. F. Crommie, Phase separation and charge transfer in a K-doped C_{60} monolayer on Ag(001). *Phys. Rev. B* **80**, 073410 (2009).
41. A. Cornia, M. Mannini, R. Sessoli, D. Gatteschi, Propeller-shaped Fe_4 and Fe_3M molecular nanomagnets: A journey from crystals to addressable single molecules. *Eur. J. Inorg. Chem.* **2019**, 552–568 (2019).
42. A. L. Barra, A. Caneschi, A. Cornia, F. de Fabrizi Biani, D. Gatteschi, C. Sangregorio, R. Sessoli, L. Sorace, Single-molecule magnet behavior of a tetranuclear iron(III) complex. The origin of slow magnetic relaxation in iron(III) clusters. *J. Am. Chem. Soc.* **121**, 5302–5310 (1999).
43. M. Mannini, F. Pineider, P. Sainctavit, L. Joly, A. Fraile-Rodríguez, M. A. Arrio, C. Cartier dit Moulin, W. Wernsdorfer, A. Cornia, D. Gatteschi, R. Sessoli, X-ray magnetic circular dichroism picks out single-molecule magnets suitable for nanodevices. *Adv. Mater.* **21**, 167–171 (2009).
44. M. Mannini, F. Pineider, C. Danieli, F. Totti, L. Sorace, P. Sainctavit, M. A. Arrio, E. Otero, L. Joly, J. C. Cezar, A. Cornia, R. Sessoli, Quantum tunnelling of the magnetization in a monolayer of oriented single-molecule magnets. *Nature* **468**, 417–421 (2010).
45. M. Mannini, E. Tancini, L. Sorace, P. Sainctavit, M. A. Arrio, Y. Qian, E. Otero, D. Chiappe, L. Margheriti, J. C. Cezar, R. Sessoli, A. Cornia, Spin structure of surface-supported single-molecule magnets from isomorphous replacement and X-ray magnetic circular dichroism. *Inorg. Chem.* **50**, 2911–2917 (2011).
46. E. Tancini, M. Mannini, P. Sainctavit, E. Otero, R. Sessoli, A. Cornia, On-surface magnetometry: The evaluation of superexchange coupling constants in surface-wired single-molecule magnets. *Chem. A Eur. J.* **19**, 16902–16905 (2013).
47. L. Malavolti, V. Lanzilotto, S. Ninova, L. Poggini, I. Cimatti, B. Cortigiani, L. Margheriti, D. Chiappe, E. Otero, P. Sainctavit, F. Totti, A. Cornia, M. Mannini, R. Sessoli, Magnetic bistability in a submonolayer of sublimated Fe_4 single-molecule magnets. *Nano Lett.* **15**, 535–541 (2015).
48. L. Gragnaniello, F. Paschke, P. Erler, P. Schmitt, N. Barth, S. Simon, H. Brune, S. Rusponi, M. Fonin, Uniaxial 2D superlattice of Fe_4 molecular magnets on graphene. *Nano Lett.* **17**, 7177–7182 (2017).
49. F. Paschke, P. Erler, V. Enenkel, L. Gragnaniello, M. Fonin, Bulk-like magnetic signature of individual Fe_4H molecular magnets on graphene. *ACS Nano* **13**, 780–785 (2019).
50. G. Serrano, L. Poggini, M. Briganti, A. L. Sorrentino, G. Cucinotta, L. Malavolti, B. Cortigiani, E. Otero, P. Sainctavit, S. Loth, F. Parenti, A. L. Barra, A. Vindigni, A. Cornia, F. Totti, M. Mannini, R. Sessoli, Quantum dynamics of a single molecule magnet on superconducting Pb(111). *Nat. Mater.* **19**, 546–551 (2020).
51. L. Poggini, E. Tancini, C. Danieli, A. L. Sorrentino, G. Serrano, A. Lunghi, L. Malavolti, G. Cucinotta, A.-L. Barra, A. Juhin, M.-A. Arrio, W. Li, E. Otero, P. Ohresser, L. Joly, J. P. Kappler, F. Totti, P. Sainctavit, A. Caneschi, R. Sessoli, A. Cornia, M. Mannini, Engineering chemisorption of Fe_4 single-molecule magnets on gold. *Adv. Mater. Interfaces* **8**, 2101182 (2021).
52. P. Erler, P. Schmitt, N. Barth, A. Irmler, S. Bouvron, T. Huhn, U. Groth, F. Pauly, L. Gragnaniello, M. Fonin, Highly ordered surface self-assembly of Fe_4 single molecule magnets. *Nano Lett.* **15**, 4546–4552 (2015).
53. F. Paschke, P. Erler, L. Gragnaniello, J. Dreiser, M. Fonin, Electrospray deposition and magnetic properties of prototypical molecular magnets. *Quantum Mater. Res.* **1**, e200002 (2020).
54. J. Tersoff, D. R. Hamann, Theory and application for the scanning tunneling microscope. *Phys. Rev. Lett.* **50**, 1998–2001 (1983).
55. F. Biedermann, H.-J. Schneider, Experimental binding energies in supramolecular complexes. *Chem. Rev.* **116**, 5216–5300 (2016).
56. D. Sertphon, P. Harding, K. S. Murray, B. Moubaraki, N. F. Chilton, S. Hill, J. Marbey, H. Adams, C. G. Davies, G. N. L. Jameson, D. J. Harding, Self-assembly of a mixed-valence Fe^{II}-Fe^{III} tetranuclear star. *Dalt. Trans.* **47**, 7118–7122 (2018).
57. G. van der Laan, A. I. Figueroa, X-ray magnetic circular dichroism—A versatile tool to study magnetism. *Coord. Chem. Rev.* **277-278**, 95–129 (2014).
58. S. Accorsi, A. L. Barra, A. Caneschi, G. Chastanet, A. Cornia, A. C. Fabretti, D. Gatteschi, C. Mortalò, E. Olivieri, F. Parenti, P. Rosa, R. Sessoli, L. Sorace, W. Wernsdorfer, L. Zobbi, Tuning anisotropy barriers in a family of tetrairon(III) single-molecule magnets with an $S = 5$ ground state. *J. Am. Chem. Soc.* **128**, 4742–4755 (2006).
59. N. Gallego-Planas, A. Martín-Rodríguez, E. Ruiz, Magnetic and transport properties of Fe_4 single-molecule magnets: A theoretical insight. *Dalt. Trans.* **45**, 18867–18875 (2016).
60. D. Gatteschi, R. Sessoli, Quantum tunneling of magnetization and related phenomena in molecular materials. *Angew. Chemie Int. Ed. Engl.* **42**, 268–297 (2003).

61. L. Gregoli, C. Danieli, A.-L. Barra, P. Neugebauer, G. Pellegrino, G. Poneti, R. Sessoli, A. Cornia, Magnetostructural correlations in tetrairon(III) single-molecule magnets. *Chem. A Eur. J.* **15**, 6456–6467 (2009).
62. P. Gambardella, S. Rusponi, M. Veronese, S. S. Dhesi, C. Grazioli, A. Dallmeyer, I. Cabria, R. Zeller, P. H. Dederichs, K. Kern, C. Carbone, H. Brune, Giant magnetic anisotropy of single cobalt atoms and nanoparticles. *Science* **300**, 1130–1133 (2003).
63. G. Fernandez Garcia, A. Lunghi, F. Totti, R. Sessoli, The disclosure of mesoscale behaviour of a 3d-SMM monolayer on Au(111) through a multilevel approach. *Nanoscale* **10**, 4096–4104 (2018).
64. F. L. Gall, F. F. de Biani, A. Caneschi, P. Cinelli, A. Cornia, A. C. Fabretti, D. Gatteschi, Synthesis, crystal structures and magnetic characterization of four β-diketonate-alkoxide iron(III) dimers. Dependence of the magnetic properties on geometrical and electronic parameters. *Inorganica Chim. Acta* **262**, 123–132 (1997).
65. V. Barone, A. Bencini, I. Ciofini, C. A. Daul, F. Totti, Density functional modeling of double exchange interactions in transition metal complexes. Calculation of the ground and excited state properties of $[Fe_2(OH)_3(tmtacn)_2]^{2+}$. *J. Am. Chem. Soc.* **120**, 8357–8365 (1998).
66. A. Lunghi, F. Totti, The role of anisotropic exchange in single molecule magnets: A CASSCF/NEVPT2 study of the Fe_4 SMM building block $[Fe_2(OCH_3)_2(dbm)_4]$ dimer. *Inorganics* **4**, 28 (2016).
67. V. Barone, A. Bencini, D. Gatteschi, F. Totti, DFT description of the magnetic properties and electron localization in dinuclear di-μ-oxo-bridged manganese complexes. *Chem. A Eur. J.* **8**, 5019–5027 (2002).
68. C. S. Yi, T. N. Zeczycki, I. A. Guzei, Highly cooperative tetrametallic ruthenium-μ-oxo-μ-hydroxo catalyst for the alcohol oxidation reaction. *Organometallics* **25**, 1047–1051 (2006).
69. H. Takezawa, T. Murase, G. Resnati, P. Metrangolo, M. Fujita, Recognition of polyfluorinated compounds through self-aggregation in a cavity. *J. Am. Chem. Soc.* **136**, 1786–1788 (2014).
70. F. Biedermann, I. Ross, O. A. Scherman, Host-guest accelerated photodimerisation of anthracene-labeled macromolecules in water. *Polym. Chem.* **5**, 5375 (2014).
71. Y. Yuan, M. F. Tam, V. Simplaceanu, C. Ho, New look at hemoglobin allostery. *Chem. Rev.* **115**, 1702–1724 (2015).
72. A. Garnovskii, B. I. Kharisov, L. M. Blanco, A. P. Sadimenko, A. I. Uraev, I. S. Vasilchenko, D. A. Garnovskii, Review: Metal complexes as ligands. *J. Coord. Chem.* **55**, 1119–1134 (2002).
73. A. S. Zyazin, J. W. G. van den Berg, E. A. Osorio, H. S. J. van der Zant, N. P. Konstantinidis, M. Leijnse, M. R. Wegewijs, F. May, W. Hofstetter, C. Danieli, A. Cornia, Electric field controlled magnetic anisotropy in a single molecule. *Nano Lett.* **10**, 3307–3311 (2010).
74. J. F. Nossa, M. F. Islam, C. M. Canali, M. R. Pederson, Electric control of a $\{Fe_4\}$ single-molecule magnet in a single-electron transistor. *Phys. Rev. B* **88**, 224423 (2013).
75. V. D. Pham, V. Repain, C. Chacon, A. Bellec, Y. Girard, S. Rousset, E. Abad, Y. J. Dappe, A. Smogunov, J. Lagoute, Tuning the electronic and dynamical properties of a molecule by atom trapping chemistry. *ACS Nano* **11**, 10742–10749 (2017).
76. A. Cini, M. Mannini, F. Totti, M. Fittipaldi, G. Spina, A. Chumakov, R. Rüffer, A. Cornia, R. Sessoli, Mössbauer spectroscopy of a monolayer of single molecule magnets. *Nat. Commun.* **9**, 480 (2018).
77. C. Wäckerlin, A. Cahlík, J. Goikoetxea, O. Stetsovych, D. Medvedeva, J. Redondo, M. Švec, B. Delley, M. Ondráček, A. Pinar, M. Blanco-Rey, J. Kolorenč, A. Arnau, P. Jelínek, Role of the magnetic anisotropy in atomic-spin sensing of 1D molecular chains. *ACS Nano* **16**, 16402–16413 (2022).
78. X. Zhang, C. Wolf, Y. Wang, H. Aubin, T. Bilgeri, P. Willke, A. J. Heinrich, T. Choi, Electron spin resonance of single iron phthalocyanine molecules and role of their non-localized spins in magnetic interactions. *Nat. Chem.* **14**, 59–65 (2022).
79. S. Rauschenbach, F. L. Stadler, E. Lunedei, N. Malinowski, S. Koltsov, G. Costantini, K. Kern, Electrospray ion beam deposition of clusters and biomolecules. *Small* **2**, 540–547 (2006).
80. A. Saywell, G. Magnano, C. J. Satterley, L. M. A. Perdigão, A. J. Britton, N. Taleb, M. del Carmen Giménez-López, N. R. Champness, J. N. O'Shea, P. H. Beton, Self-assembled aggregates formed by single-molecule magnets on a gold surface. *Nat. Commun.* **1**, 75 (2010).
81. R. Feenstra, J. A. Stroscio, A. Fein, Tunneling spectroscopy of the Si(111)2x1 surface. *Surf. Sci.* **181**, 295–306 (1987).
82. C. Piamonteze, U. Flechsig, S. Rusponi, J. Dreiser, J. Heidler, M. Schmidt, R. Wetter, M. Calvi, T. Schmidt, H. Pruchova, J. Krempasky, C. Quitmann, H. Brune, F. Nolting, X-Treme beamline at SLS: X-ray magnetic circular and linear dichroism at high field and low temperature. *J. Synchrotron Radiat.* **19**, 661–674 (2012).
83. T. D. Kühne, M. Iannuzzi, M. del Ben, V. V. Rybkin, P. Seewald, F. Stein, T. Laino, R. Z. Khaliullin, O. Schütt, F. Schiffmann, D. Golze, J. Wilhelm, S. Chulkov, M. H. Bani-Hashemian, V. Weber, U. Borštnik, M. Taillefumier, A. S. Jakobovits, A. Lazzaro, H. Pabst, T. Müller, R. Schade, M. Guidon, S. Andermatt, N. Holmberg, G. K. Schenter, A. Hehn, A. Bussy, F. Belleflamme, G. Tabacchi, A. Glöß, M. Lass, I. Bethune, C. J. Mundy, C. Plessl, M. Watkins, J. VandeVondele, M. Krack, J. Hutter, CP2K: An electronic structure and molecular dynamics software package—Quickstep: Efficient and accurate electronic structure calculations. *J. Chem. Phys.* **152**, 194103 (2020).
84. J. P. Perdew, K. Burke, M. Ernzerhof, Generalized gradient approximation made simple. *Phys. Rev. Lett.* **77**, 3865–3868 (1996).
85. Y. Zhang, W. Yang, Comment on "Generalized Gradient Approximation Made Simple". *Phys. Rev. Lett.* **80**, 890–890 (1998).
86. R. Sabatini, T. Gorni, S. de Gironcoli, Nonlocal van der Waals density functional made simple and efficient. *Phys. Rev. B* **87**, 041108 (2013).
87. S. Goedecker, M. Teter, J. Hutter, Separable dual-space Gaussian pseudopotentials. *Phys. Rev. B* **54**, 1703–1710 (1996).
88. V. Corradini, A. Ghirri, U. del Pennino, R. Biagi, V. A. Milway, G. Timco, F. Tuna, R. E. P. Winpenny, M. Affronte, Grafting molecular Cr_7Ni rings on a gold surface. *Dalt. Trans.* **39**, 4928 (2010).
89. S. Kahle, Z. Deng, N. Malinowski, C. Tonnoir, A. Forment-Aliaga, N. Thontasen, G. Rinke, D. Le, V. Turkowski, T. S. Rahman, S. Rauschenbach, M. Ternes, K. Kern, The quantum magnetism of individual manganese-12-acetate molecular magnets anchored at surfaces. *Nano Lett.* **12**, 518–521 (2012).
90. F. Paschke, T. Birk, V. Enenkel, F. Liu, V. Romankov, J. Dreiser, A. A. Popov, M. Fonin, Exceptionally high blocking temperature of 17 K in a surface-supported molecular magnet. *Adv. Mater.* **33**, 2102844 (2021).
91. F. Paschke, "Control and manipulation of electronic and spin states in individual molecular magnets," thesis, Universität Konstanz, Konstanz (2022).
92. Y. Qi, X. Ma, P. Jiang, S. Ji, Y. Fu, J. F. Jia, Q. K. Xue, S. B. Zhang, Atomic-layer-resolved local work functions of Pb thin films and their dependence on quantum well states. *Appl. Phys. Lett.* **90**, 013109 (2007).
93. D. Niesner, T. Fauster, J. I. Dadap, N. Zaki, K. R. Knox, P. C. Yeh, R. Bhandari, R. M. Osgood, M. Petrović, M. Kralj, Trapping surface electrons on graphene layers and islands. *Phys. Rev. B* **85**, 081402 (2012).
94. P. Järvinen, S. K. Hämäläinen, K. Banerjee, P. Häkkinen, M. Ijäs, A. Harju, P. Liljeroth, Molecular self-assembly on graphene on SiO_2 and h-BN substrates. *Nano Lett.* **13**, 3199–3204 (2013).
95. B. T. Thole, P. Carra, F. Sette, G. van der Laan, X-ray circular dichroism as a probe of orbital magnetization. *Phys. Rev. Lett.* **68**, 1943–1946 (1992).
96. P. Carra, B. T. Thole, M. Altarelli, X. Wang, X-ray circular dichroism and local magnetic fields. *Phys. Rev. Lett.* **70**, 694–697 (1993).
97. R. Wu, A. J. Freeman, Limitation of the magnetic-circular-dichroism spin sum rule for transition metals and importance of the magnetic dipole term. *Phys. Rev. Lett.* **73**, 1994–1997 (1994).
98. M. Retegan, mretegan/crispy: v0.8.0, doi:10.5281/ZENODO.13845266, https://zenodo.org/records/13845266.
99. S. L. Dudarev, G. A. Botton, S. Y. Savrasov, C. J. Humphreys, A. P. Sutton, Electron-energy-loss spectra and the structural stability of nickel oxide: An LSDA+U study. *Phys. Rev. B* **57**, 1505–1509 (1998).
100. S. Ninova, V. Lanzilotto, L. Malavolti, L. Rigamonti, B. Cortigiani, M. Mannini, F. Totti, R. Sessoli, Valence electronic structure of sublimated Fe_4 single-molecule magnets: An experimental and theoretical characterization. *J. Mater. Chem. C* **2**, 9599–9608 (2014).
101. L. Noodleman, Valence bond description of antiferromagnetic coupling in transition metal dimers. *J. Chem. Phys.* **74**, 5737–5743 (1981).
102. A. Bencini, F. Totti, A few comments on the application of density functional theory to the calculation of the magnetic structure of oligo-nuclear transition metal clusters. *J. Chem. Theory Comput.* **5**, 144–154 (2009).
103. F. Neese, Software update: The ORCA program system, version 4.0. *WIREs Comput. Mol. Sci.* **8**, (2018).
104. A. Lunghi, M. Iannuzzi, R. Sessoli, F. Totti, Single molecule magnets grafted on gold: Magnetic properties from ab initio molecular dynamics. *J. Mater. Chem. C* **3**, 7294–7304 (2015).
105. F. Weigend, R. Ahlrichs, Balanced basis sets of split valence, triple zeta valence and quadruple zeta valence quality for H to Rn: Design and assessment of accuracy. *Phys. Chem. Chem. Phys.* **7**, 3297–3305 (2005).
106. S. Schmitt, P. Jost, C. van Wüllen, Zero-field splittings from density functional calculations: Analysis and improvement of known methods. *J. Chem. Phys.* **134**, 194113 (2011).
107. A. Lunghi, F. Totti, DFT magnetic characterization of a Fe_4 SMMs series: From isotropic exchange interactions to multi-spin zero field splitting. *J. Mater. Chem. C* **2**, 8333–8343 (2014).
108. K. Kambe, On the paramagnetic susceptibilities of some polynuclear complex salts. *J. Physical Soc. Japan* **5**, 48–51 (1950).
109. D. Gatteschi, R. Sessoli, J. Villain, *Molecular Nanomagnets* (Oxford Univ. Press, 2011).
110. R. Boča, *Theoretical Foundations of Molecular Magnetism* (Elsevier, 1999).
111. A. Bencini, D. Gatteschi, *Electron Paramagnetic Resonance of Exchange Coupled Systems* (Springer Berlin Heidelberg, 1990).

Acknowledgments
Funding: M.F. acknowledges financial support by the Deutsche Forschungsgemeinschaft (DFG)—FO 640/7-1 and SFB 1432 (project no. 425217212). This work was supported by the European Union through the Next Generation EU funds through the Italian MUR National Recovery and Resilience Plan, Mission 4 Component 2 - Investment 1.4 - National Center for HPC, Big Data, and Quantum Computing (CUP B83C22002830001). We furthermore acknowledge the support of MUR through Progetto Dipartimenti di Eccellenza 2018–2022 (CUP B96C1700020008) and 2023–2027 (CUP B97G22000740001 - DICUS 2.0). **Author contributions:** M.F. conceptualized and supervised the project. F.P., V.E., and T.B. performed sample preparation and STM characterization. F.P., V.E., T.B., J.D., and M.F. carried out the XAS and XMCD measurements. M.B. and F.T. carried out first-principle calculations and rationalization of experimental data. P.S. synthesized the molecules. R.F.W. supervised the project. F.P., M.B., F.T., and M.F. drafted the manuscript. All authors discussed the results and contributed to writing the paper. **Competing interests:** The authors declare that they have no competing interests. **Data and materials availability:** All data needed to evaluate the conclusions in the paper are present in the paper and/or the Supplementary Materials.

Submitted 23 October 2024
Accepted 14 April 2025
Published 23 May 2025
10.1126/sciadv.adu0916